

Experimental and Numerical Study of Dynamic Fragmentation in Laser Shock-Loaded Gold and Aluminium Targets

E. Lescoute¹, T. De Ressaigui¹, J.-M. Chevalier², J. Breil³
P.-H. Maire², and G. Schurtz³

Abstract: With the ongoing development of high energy laser facilities designed to achieve inertial confinement fusion, the ability to simulate debris ejection from metallic shells subjected to intense laser irradiation has become a key issue. We present an experimental and numerical study of fragmentation processes generating high velocity ejecta from laser shock-loaded metallic targets (aluminium and gold). Optical transverse shadowgraphy is used to observe and analyze dynamic fragmentation and debris ejection. Experimental results are compared to computations involving a fragmentation model based on a probabilistic description of material tensile strength. A correct overall consistency is obtained.

Keywords: Shock, fragmentation, spallation, laser, gold, aluminium.

1 Introduction

The capability to simulate and to predict shrapnel generation and ejection in complex geometries is an issue of considerable importance in the development of high energy laser facilities dedicated to inertial confinement fusion, such as the Laser MégaJoule in France or the National Ignition Facility in the USA, where metallic shells will be subjected to intense laser irradiation. In the promising configuration known as indirect drive [J. D. Lindl et al. (2004)], a gold hohlraum will be irradiated simultaneously by several tens of high power laser beams with a pulse duration of a few ns, which will generate a variety of fragments. In order to extend the facility lifetime and to design suitable protections, it is crucial to be able to anticipate the

¹ Institut PPRIME, UPR 3346, CNRS, ENSMA, Université de Poitiers, 1 av. Clément Ader, 86961 Futuroscope Cedex, France

² CEA - CESTA, BP 2 - 33114 Le Barp Cedex - France

³ CELIA - CEA/CNRS/Université Bordeaux I - 351 Cours de la Libération - 33405 Talence Cedex - France

ballistic properties of these fragments and the damage that their impact might cause to the nearby equipments.

The heating of a metallic target by a high power laser pulse produces the ablation of a thin layer of material, whose expansion induces by reaction a compressive pulse into the solid sample. During its propagation in the material, the compression front gets steeper and the unloading wave spreads. Consequently, the pressure pulse becomes a roughly triangular, "unsupported" shock wave, and the peak pressure decays with increasing propagation distance (Fig. 1).

In such laser shock-loaded solid target, two main processes, depending on the sample thickness, are expected to generate high velocity ejecta: spallation (Fig. 1) and thin foil fragmentation (Fig. 2). In a thick target (Fig. 1), when the compressive pulse reflects from the opposite free surface, tensile stresses are induced by the interaction of incident and reflected release waves within the sample. Spall damage is initiated, growing to full fracture, then fragments (spalled layers) are ejected from the sample. Spallation has been widely studied in the past under explosive loading and plate impact [e.g. M. A. Meyers and C. T. Aimone (1983); L. Davison et al. (1996); T. Antoun et al. (2002)], and for a few decades under laser shock-loading [S. Eliezer et al. (1990a,b); M. Boustie and F. Cottet (1991); T. De Ressaiguier et al. (1997); L. Tollier and R. Fabbro (1998); M. A. Meyers et al. (2001); T. De Ressaiguier and M. Hallouin (2008)]. In a thin target (i.e. some tens of micrometers or less) (Fig. 2), the duration of pressure application on the irradiated surface is longer than the time taken by the pressure waves to propagate through the sample to the free surface then back to the loaded surface. In this case, pressure decay during propagation through the foil is much less than in a thick target, which leads to much higher peak velocity upon shock breakout at the free surface for a given laser pulse. Moreover successive reaccelerations of the foil occur as long as the expanding plasma exerts a pressure on the loaded surface, which leads to high overall deformation that can be referred to as dynamic punching.

In this paper, we present an experimental and numerical investigation of both fragmentation processes in metallic samples (gold and aluminium) under intense laser irradiation in nanosecond regime. Experimental results consist in transverse optical shadowgraphy of ejected debris. They are compared with numerical predictions accounting for laser-matter interaction, wave propagation and spall fracture. Fragmentation is modelled using a simple erosion criterion and a random distribution of pre-existing defects in the material.

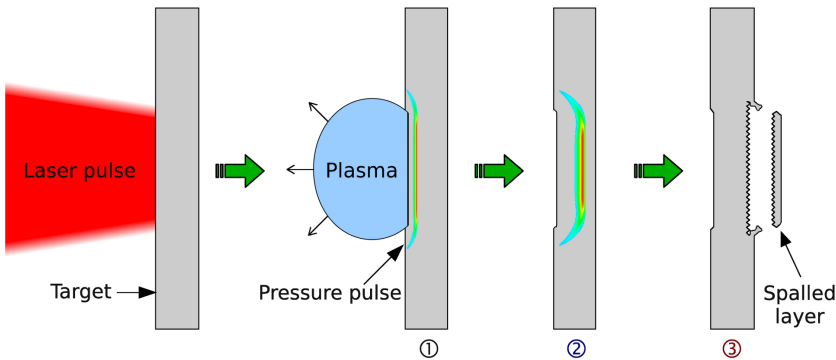


Figure 1: Phenomenological description of laser shock-induced spallation. (1) A pressure pulse is induced by the expansion of the ablation plasma. (2) Because the compression front gets steeper, the pressure pulse becomes a triangular shock wave. (3) A spalled layer is generated when the negative pressure induced by the reflection of the compressive pulse from the free surface overcomes the dynamic strength of the material.

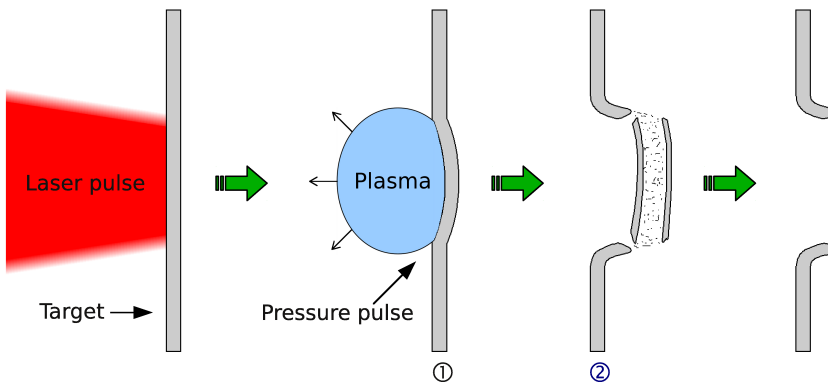


Figure 2: Phenomenological description of thin foil fragmentation by laser irradiation. (1) A pressure pulse is induced by the ablation plasma expansion. (2) In addition to spallation which can occur, dynamic punching leads to the ejection of various fragments and results in a large hole in the foil.

2 Experiments

Experiments have been performed in the *Centre d'Études Scientifiques et Techniques d'Aquitaine* (CESTA, CEA, *Alisé* facility, France) on aluminium and gold targets of thicknesses ranging from 200 to 300 μm . Targets are placed in a vacuum

chamber and impacted by a high power laser pulse (Nd:Glass) of 1.06 μm wavelength focused onto a spot of 2 mm diameter (Fig. 3). The pulse duration and maximum laser energy are 3 ns and 180 J, and the corresponding peak laser intensity is $2 \times 10^{12} \text{ W/cm}^2$.

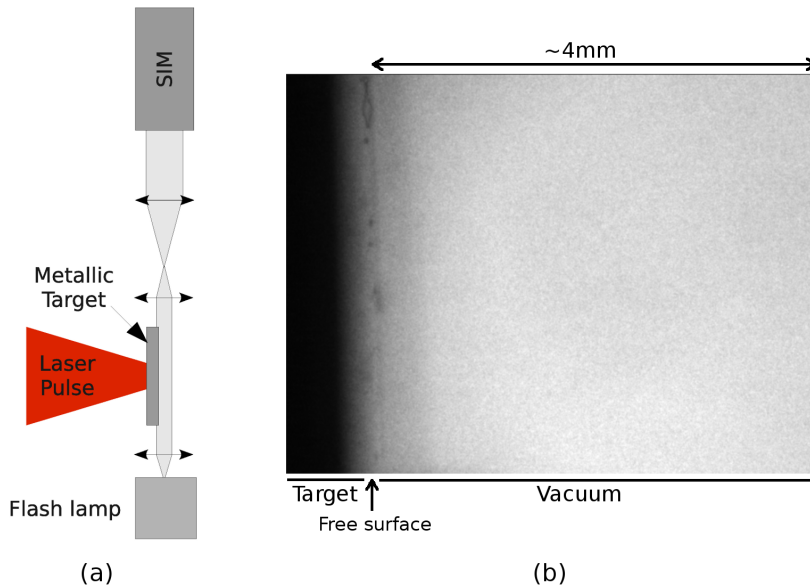


Figure 3: (a) Schematic of the experimental setup. Ejecta generated from laser shock loading are observed using optical shadowgraphy. A fast camera (SIM) performs 8 acquisitions with a minimum interframe delay of 3 ns. (b) Example of reference shadowgraph recorded before a laser shot. The target is on the left, and the gap observed behind the free surface is about 4 mm.

Dynamic fragmentation and debris ejection are investigated using optical transverse shadowgraphy (Fig. 3), which gives quasi-instantaneous images of the ejected fragments at controlled delay times after the laser shot [E. Lescoute et al. (2009a,b)]. Transverse illumination is provided by a flash lamp, which emits an incoherent white light. A fast camera developed by *Specialised Imaging*¹ (SIM) records 8 frames with an independently adjustable gain for each frame, a minimum interframe time of 3 ns and a minimum exposure time of 5 ns. The resulting motion blur for the fastest ejecta ($\sim 2000 \text{ m/s}$) is typically $10 \mu\text{m}$, which corresponds to about 3 pixels on the camera chip.

¹ www.specialised-imaging.com

From a broad series of shots to be reported in a forthcoming paper [E. Lescoute et al. (2010)], four experiments are chosen here for their pertinence in the present work. The main experimental parameters and results are summarized in Table 1.

Table 1: Summary of the main experimental results. Shock loading and breakout pressures are calculated from simulation of laser-matter interaction and wave propagation, mean velocity of the fastest ejecta (i.e. front of the debris cloud) is derived from transverse shadowgraphs, and spall strength is inferred from time-resolved velocity measurements [E. Lescoute et al. (2010)]

Material	Sample thickness (μm)	Laser intensity (TW/cm^2)	Peak loading pressure (GPa)	Shock breakout pressure (GPa)	Max ejecta velocity (m/s)	Measured spall strength (GPa)
Al	200	1.27	46	21	1698	2.0
Al	20	1.81	61	54	> 4000	-
Au	300	1.98	47	15	310	4.1
Au	20	1.58	36	35	809	-

3 Numerical modelling

Numerical simulations have been performed with the two-dimensional hydrodynamic code CHIC² [P.-H. Maire et al. (2008); P.-H. Maire and J. Breil (2008)] developed in the *Centre Lasers Intenses et Applications* (CELIA), that solves the standard conservation equations for mass, momentum and energy written in Lagrangian formalism. The underlying numerical scheme is based on a high-order cell-centered discretization of Lagrangian hydrodynamics [P.-H. Maire (2009)]. The laser absorption is calculated by inverse bremsstrahlung.

² Code Hydrodynamique et d'Implosion du CELIA

To simulate a laser shot, the temporal shape of the loading pressure pulse is calculated from a one-dimensional computation of laser-matter interaction, using the measured laser data (energy, pulse temporal profile) and a very fine spatial discretization. The pressure history calculated in the cell representing vapour/solid interface (typically a few hundreds of nanometers-deep below the irradiated surface) is considered as the pressure load. Then, this computed pressure pulse is applied as a boundary condition in a two-dimensional simulation, assuming an homogeneous spatial distribution of the laser energy over the irradiated surface, and using a coarser mesh to discretize the whole sample section. Materials hydrodynamics are described with Bushman Lomonosov Fortov (BLF) [A. V. Bushman et al. (1992, 1993)] tabulated equations of state (EOS).

Spall fracture is modelled using a simple erosion criterion assuming instantaneous element deletion as soon as the local tensile stress (negative pressure) reaches a threshold strength:

$$\sigma \geq \sigma_c \Rightarrow \text{rupture} \quad (1)$$

To numerically delete the element, some variables are set to zero, including the pressure, the thermal conductivity, the internal energy and the density. In an homogeneous, isotropic material, σ_c is considered as a constant parameter, identical for all cells. However, such perfect uniformity is unrealistic in a real polycrystalline specimen, where grain boundaries, impurities or defects introduce weaker spots. Several probabilistic approaches have been proposed to model dynamic fragmentation of ductile [C. Czarnota et al. (2008); H. Trumel et al. (2009)] and brittle materials [C. Denoual et al. (1997)], or crack propagation in brittle materials [V. V. Silberschmidt (2003, 2006)].

Here, as a preliminary attempt to account for such defaults in the material, the spall strength value has been assigned through a gaussian distribution centered on a reference value σ_{ref} (Fig. 4), and randomly distributed in the target section, using the Box-Muller algorithm [G. E. P. Box and M. E. Muller (1958)]:

$$\sigma_c = \sigma_{ref} \left(1 + \frac{\delta}{2} \sqrt{-2 \log(u_1) \cos(2\pi u_2)} \right) \quad (2)$$

where $\delta \times \sigma_{ref}$ is the full width at half maximum, and u_1 and u_2 are random values between 0 and 1, such as $0 < u_{1,2} < 1$. σ_{ref} has been set to a mean experimental value given in Table 1, determined from time-resolved measurements of the free surface velocity [T. Antoun et al. (2002); E. Lescoute et al. (2010)]

However the failure criterion (Eq. 1) is never met in elements located at free surfaces, where the pressure is set to zero as a boundary condition, even if elongation

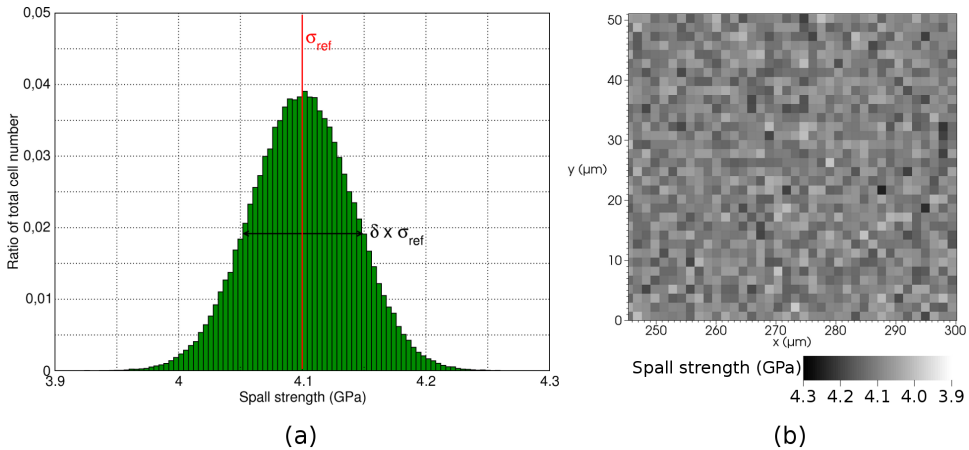


Figure 4: (a) Gaussian distribution of the spall strength value with $\delta = 0.02$ and $\sigma_{ref} = 4.1 \times 10^9$ Pa. (b) Partial view of a target where spall strength values are randomly distributed.

or deformation increase dramatically. Thus, a numerical deformation criterion has been added to detect non-physical geometries. The element is deleted if the ratio between its two main characteristic dimensions is higher than a prescribed threshold. As it will be shown in Section 4.2, this criterion allows modelling the full separation of the spalled layers from the unspalled part of the target.

4 Spallation of thick targets

4.1 Experimental results

Fig. 5 shows an example of transverse shadowgraphs obtained with the SIM camera behind a $300 \mu\text{m}$ -thick gold target impacted with a $1.98 \text{ TW}/\text{cm}^2$ laser shot corresponding to a 47 GPa peak loading pressure and a 15 GPa shock breakout pressure at the free surface (Table 1). After the shock breakout, which leads to a deformation of the free surface (visible on the first frame), a planar spalled layer is ejected with a mean velocity of $310 \pm 8 \text{ m/s}$ (inferred from successive frames). This first spalled layer has an apparent thickness larger than the target thickness, due to important curvature at the periphery before its separation from the target. Slower fragments are visible behind the main spall, which can be explained by two processes. First, the separation of the main spall can produce small fragments in the peripheral zones. Second, upon reflection of the triangular pressure pulse from the free surface, multiple spallation [J. S. Rinehart (1952)] is expected to generate suc-

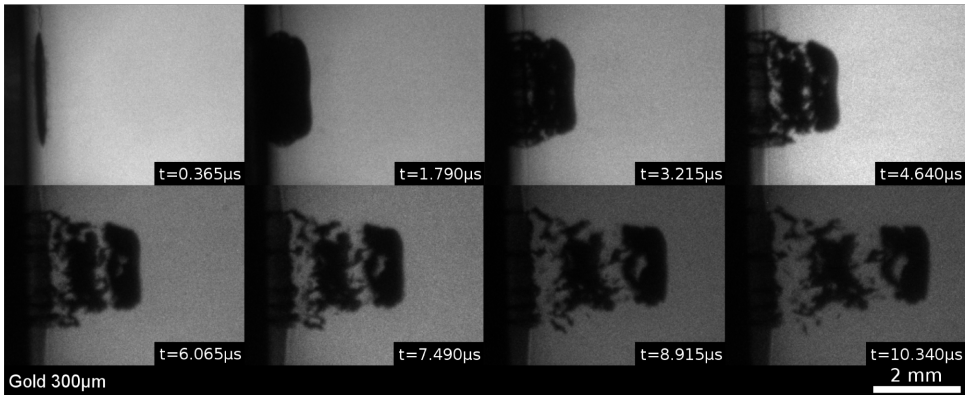


Figure 5: Visualization of the fragments ejection from a 300 μm -thick gold target subjected to a 47 GPa laser shock. The delay time between two successive pictures is 1.425 μs and the exposure time for each frame is 10 ns. The shock was applied from left to right. The ejection velocity of the first spalled layer is 310 ± 8 m/s.

cessive spalled layers slower than the first one. Actually, in laser shock experiments where dimensions are of μm -order, secondary fracture would more likely produce irregular, distinct fragments, instead of successive planar layers.

An example of transverse visualization obtained in a similar experiment on a 200 μm -thick aluminium target with a laser intensity of $1.27 \text{ TW}/\text{cm}^2$ is shown in Fig. 6. The loading pressure near the irradiated surface is 46 GPa, and the shock breakout pressure is 21 GPa (Table 1). The first spalled layer is ejected from the free surface with a mean ejection velocity of 1698 ± 42 m/s. It is followed by a large amount of secondary fragments leading to the expansion of a cloud of small debris. Such difference from the case of gold can be explained by the lower spall strength of aluminium.

4.2 Numerical simulations

Fig. 7 and 8 show two simulations of the experiment presented in Fig. 5. Half of the target has been discretized into 160000 square cells of 1.5 μm side length. The mean spall strength of laser shock-loaded gold has been determined as 4.1 GPa [E. Lescoute et al. (2010)], which is taken as the σ_{ref} value. In Fig. 7, the sample is considered as perfectly homogeneous, so that $\sigma_c = \sigma_{ref}$ in all elements. Planar spall fractures are well reproduced by the traction criterion (Eq. 1) and occur a few tens of μm beneath the free surface (Fig. 7a). Then, because of important deformation at the periphery, a first spalled layer is ejected from the target (Fig. 7b) with a mean ejection velocity of 296 m/s is in very good agreement with the experiment

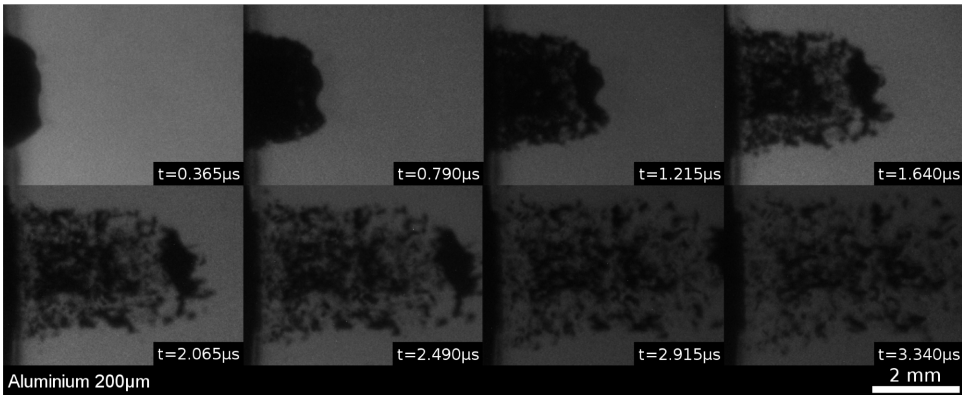


Figure 6: Visualization of the fragments ejection from a 200 μm -thick aluminium target subjected to a 46 GPa laser shock. The delay time between two successive pictures is 0.285 μs and the exposure time for each frame is 10 ns. The shock was applied from left to right. The ejection velocity of the first spalled layer is 1698 ± 42 m/s.

(310 m/s, see Table 1). In the elements located at the periphery, it is not possible to obtain a correct computed traction because of their proximity with the free surfaces. Consequently, the separation of the spalled layer from the unspalled target is due to the deformation criterion. A second spalled layer is ejected behind the first one, and secondary fragments are produced near the edges (Fig. 7c). These predictions are qualitatively consistent with the shadowgraphs (Fig. 5). However, because of the assumption of a perfectly homogeneous target, the computed rupture remains one-dimensional in the central zone. To perform a more realistic simulation, the presence of defects can be taken into account in the target, through a non-uniform spall strength distribution as discussed in Section 3. In Fig. 8, spall strength values of $4.1 \text{ GPa} \pm 1\%$ (Fig. 4), have been randomly distributed in elements. This simple probabilistic description leads to discontinuous fractures beneath the free surface (Fig. 8a) which result in the separation of a first non-planar spalled layer (Fig. 8b) and in the generation of distinct, slower fragments (Fig. 8c). This result seems to be more consistent than the previous one with transverse shadowgraphs, where small fragments can be distinguished behind the main spalled layer. In this simulation, the first spalled layer is ejected with a mean velocity of 270 m/s, lower than the previous one, because later fractures at stronger spots within the target have delayed the separation of the spall. However, the discrepancy between this lower velocity and the measured one is about 13 %, which remains within the overall experimental uncertainty.

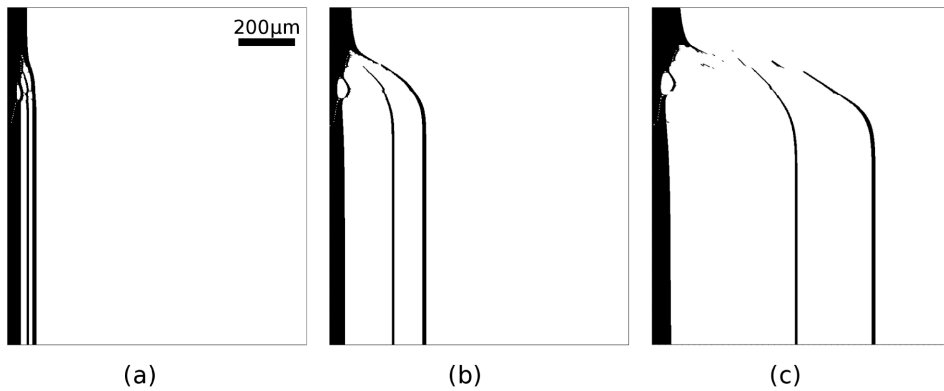


Figure 7: Partial views of the 2D axisymmetric simulation of a 47 GPa laser shock on a 300 μm -thick gold target corresponding to the Fig. 5. The pressure load is applied on the left surface (not shown) over a 1 mm radius spot. Target is plotted 200 ns (a), 1000 ns (b), and 2500 ns (c) after the laser shot. The first spalled layer is ejected with a mean velocity of 296 m/s. The final proportion of deleted elements is 1.1 %.

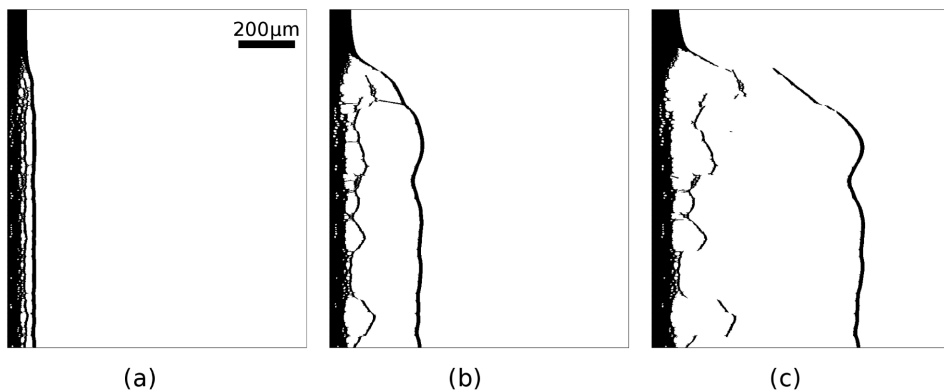


Figure 8: Partial views of the 2D axisymmetric simulation of a 47 GPa laser shock on a 300 μm -thick gold target corresponding to the Fig. 5. The pressure load is applied on the left surface (not shown) over a 1 mm radius spot. Target is plotted 200 ns (a), 1000 ns (b), and 2500 ns (c) after the laser shot. The first spalled layer is ejected with a mean velocity of 270 m/s. The final proportion of deleted elements is 1.4 %.

Fig. 9 and 10 show similar simulations of the experiment presented in Fig. 6 on an aluminium target discretized into 106400 square cells of $1.5\ \mu\text{m}$ side length, using a spall strength of 2.0 GPa in Fig. 9 and $2.0\ \text{GPa} \pm 1\%$ in Fig. 10. First spalled layers are ejected with mean velocities of 1708 m/s (Fig. 9) and 1605 m/s (Fig. 6) (1698 m/s in the experiment). Like in the case of gold, distinct fragments are generated with the variable spall strength, and because of a lower nominal value σ_{ref} , the number of secondary layers is higher than in gold, which is consistent with the experimental observations (Fig. 6).

5 Thin foils fragmentation

5.1 Experimental results

Similar laser shots have been performed on $20\ \mu\text{m}$ -thick gold targets. The optical shadowgraphs in Fig. 11 show the early rupture of the target and the ejection of a cloud of thin debris with a maximum velocity of 809 m/s. The peak loading pressure induced by the laser impact at $1.58\ \text{TW}/\text{cm}^2$ is 36 GPa. Pressure decay during propagation throughout such thin foils is weak, so that the shock breakout pressure is 35 GPa beneath the free surface. A group of faster fragments can be distinguished in the shadowgraphs, ahead of the dark expanding cloud. They can be attributed to a fragmented spalled layer. After the ejection of this spall, dynamic punching generates lateral tensions and the formation of a multitude of slower micrometric fragments, with a wide range of velocities leading to a continuous debris cloud.

Optical shadowgraphs obtained in a similar experiment on a $20\ \mu\text{m}$ -thick aluminium target are shown in Fig. 12. The laser intensity is $1.81\ \text{TW}/\text{cm}^2$. The corresponding peak loading pressure is 61 GPa and the shock breakout pressure is 54 GPa. In this case, the maximum ejection velocity of fragments, much higher than in gold, could not be exactly measured. It has been estimated to about 4200 m/s.

5.2 Numerical simulations

Fig. 13 shows the numerical simulation of the experiment presented in Fig. 11. The whole target section has been discretized in 57000 square cells of $1\ \mu\text{m}$ side length. A spall strength of $4.1\ \text{GPa} \pm 1\%$, randomly distributed in the target has been used. Fragmentation results from a combination of spallation, with the ejection of a first spalled layer ejected at about 800 m/s followed by a multitude of distinct, micrometric fragments (Fig. 13a), and punching, with the formation of a large hole in the foil (Fig. 13c).

Fig. 14 shows the simulation of the experiment presented in Fig. 12 on an aluminium target, using a spall strength of $2.0\ \text{GPa} \pm 1\%$. Like in gold, a first spalled

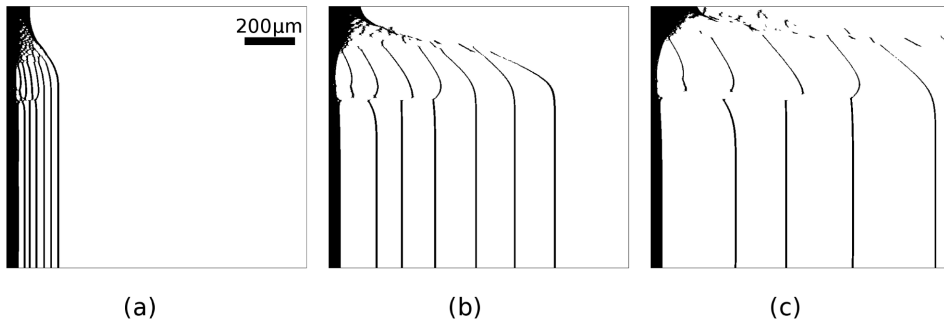


Figure 9: Partial views of the 2D axisymmetric simulation of a 46 GPa laser shock on a 200 μm -thick aluminium target corresponding to the Fig. 6. The pressure load is applied on the left surface (not shown) over a 1 mm radius spot. Target is plotted 100 ns (a), 500 ns (b), and 1000 ns (c) after the laser shot. The first spalled layer is ejected with a mean velocity of 1708 m/s. The final proportion of deleted elements is 6.0 %.

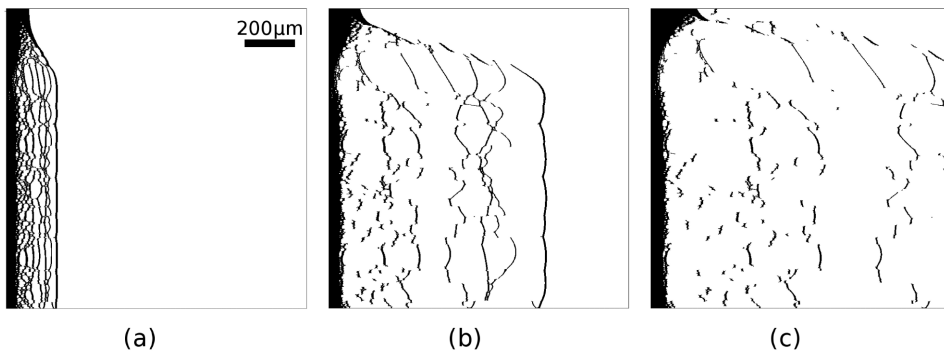


Figure 10: Partial views of the 2D axisymmetric simulation of a 46 GPa laser shock on a 200 μm -thick aluminium target corresponding to the Fig. 6. The pressure load is applied on the left surface (not shown) over a 1 mm radius spot. Target is plotted 100 ns (a), 500 ns (b), and 1000 ns (c) after the laser shot. The first spalled layer is ejected with a mean velocity of 1605 m/s. The final proportion of deleted elements is 9.9 %.

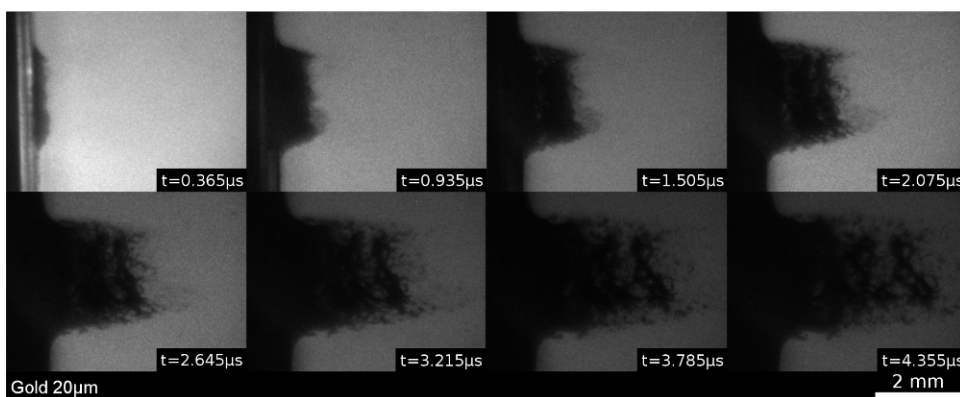


Figure 11: Visualization of the fragments ejection from a 20 μm -thick gold target subjected to a 36 GPa laser shock. The delay time between two successive pictures is $0.570 \mu\text{s}$ and the exposure time for each frame is 5 ns. The shock was applied from left to right. The ejection velocity of the fastest fragments is $809 \pm 41 \text{ m/s}$.

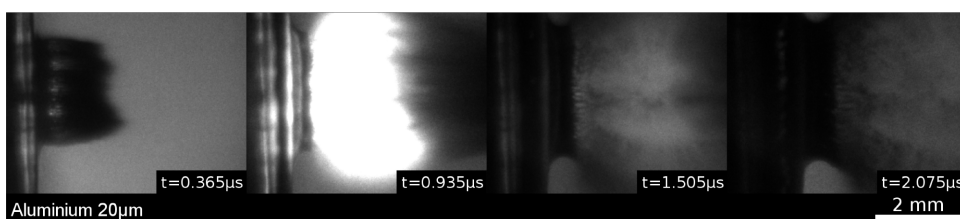


Figure 12: Visualization of the fragments ejection from a 20 μm -thick aluminium target subjected to a 61 GPa laser shock. The delay time between two successive pictures is $0.570 \mu\text{s}$ and the exposure time for each frame is 5 ns. The shock was applied from left to right. The ejection velocity of the fastest fragments is higher than 4000 m/s . In the second frame, the saturation of a part of the chip camera is due to radiant particles coming from the loaded side through a hole that has formed in the punched target.

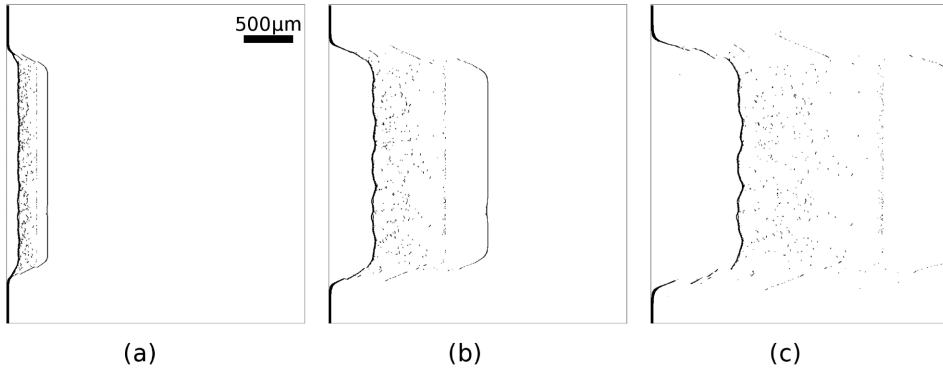


Figure 13: Views of the 2D simulation of a 36 GPa laser shock on a 20 μm -thick gold target corresponding to the Fig. 11. The pressure load is applied on the left surface over a 1 mm radius spot. Target is plotted 500 ns (a), 2000 ns (b), and 4000 ns (c) after the laser shot. The first spalled layer is ejected with a mean velocity of 800 m/s. The final proportion of deleted elements is 18.6 %.

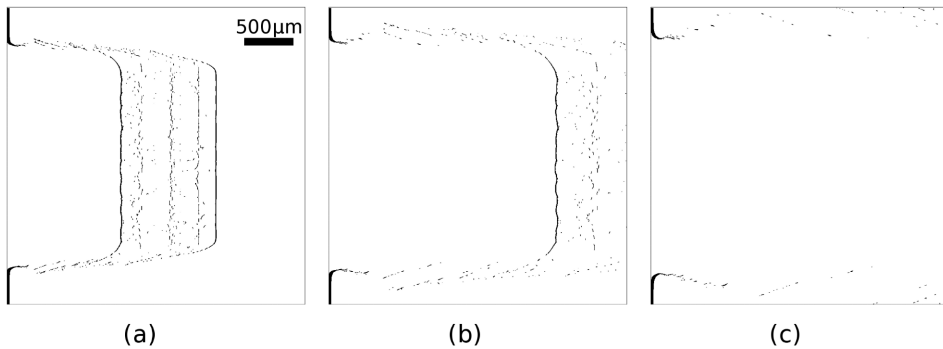


Figure 14: Views of the 2D simulation of a 61 GPa laser shock on a 20 μm -thick aluminium target corresponding to the Fig. 12. The pressure load is applied on the left surface over a 1 mm radius spot. Target is plotted 500 ns (a), 1000 ns (b), and 2000 ns (c) after the laser shot. The first spalled layer is ejected with a mean velocity of 4230 m/s. The final proportion of deleted elements is 24.5 %.

layer is ejected followed by a cloud of fragments and opening of the foil due to dynamic punching. The mean ejection velocity of the first spalled layer is 4230 m/s.

6 Discussion

The results presented above illustrate the coupling of laser shock experiments and numerical simulations to investigate shock-induced fragmentation processes in gold and aluminium at high strain rates of the order of 10^6 - 10^7 s⁻¹. Experimental results consist in transverse shadowgraphy of target deformation and fragments ejection. In thick targets, a first spalled layer is ejected, followed by secondary fragments with size, number and velocity depending on the material and the loading pressure. Such secondary fragments are mostly due to multiple spallation and to the late separation of the spalled layer from the target. In thin foils, dynamic punching leads to the ejection of a multitude of fragments of various sizes and to the opening of the target with the formation of a large central hole.

Numerical simulations have been performed with a two-dimensional hydrocode using a simple erosion criterion to model instantaneous fracture above a threshold tensile strength, complemented by an additional erosion of elements assumed to reach non-physical deformations. Because the pressure load is assumed to be uniform over a surface of diameter considerably greater than the sample thickness, conditions of uniaxial strain are induced near the symmetry axis, while edge effects are limited to small peripheral zones. Thus, if the tensile strength is assumed to be uniform within a perfectly homogenous material, computed damage is essentially limited to planar fracture. To depart from this one-dimensional fragmentation and aim at more realistic simulations, the presence of pre-existing defects in the material has been introduced using a gaussian distribution of the spall strength value randomly allocated in the target section. As a result, non-planar fractures are created, leading to the generation and the ejection of a variety of fragments in better qualitative agreement with the observations. Indeed, a correct overall consistency is obtained for the four experimental cases, as illustrated in the comparisons shown in Appendix A.

However, the numerical approach presented here is only a preliminary attempt to account for any real material non-uniformity, such as that induced by defects or grain boundaries. In particular, two major limitations of this approach will have to be overcome in future work: (i) the characteristic size and spacing of the inhomogeneities are presently constrained to the element size (μm -order), probably too small to be physically representative, and (ii) 2D simulations do not provide the volume of generated fragments, which will require computations with a 3D code.

Furthermore, parametric and/or experimental studies should be performed for a

more relevant determination of the parameter δ in Eq. 2 governing the variations of the spall strength.

Acknowledgement: We thank all the staff of Alisé for technical support, as well as our co-workers from Institut PPRIME and PIMM who took part in the laser experiments. We particularly thank Mr. Wai Chan from Specialised Imaging Company for providing and helping us to run the SIM camera.

References

- A. V. Bushman et al.** (1992): Equation of state of metals at high energy densities. Russian academy of sciences, Institute of Chemical Physics, Chernogolovka, 1992.
- A. V. Bushman et al.** (1993): Models of wide-range equations of state for matter under conditions of high energy density. *Sov. Tech. Rev. B*, , no. 5, pp. 1.
- C. Czarnota et al.** (2008): Modelling of dynamic ductile fracture and application to the simulation of plate impact tests on tantalum. *Journal of the Mechanics and Physics of Solids*, vol. 56, no. 4, pp. 1624 – 1650.
- C. Denoual et al.** (1997): A statistical approach for fragmentation of brittle materials under dynamic loading. *C. R. Acad. Sci. Paris-Series IIB*, vol. 325, no. 12, pp. 685–691.
- E. Lescoute et al.** (2009): Soft recovery technique to investigate dynamic fragmentation of laser shock-loaded metals. *Applied Physics Letters*, vol. 95, pp. 211905.
- E. Lescoute et al.** (2009): Transverse shadowgraphy and new recovery techniques to investigate dynamic fragmentation of laser shock-loaded metals. *Shock compression of condensed matter*.
- E. Lescoute et al.** (2010): Ejection of spalled layers from laser shock-loaded metals. *J. Appl. Phys.*, vol. 108, pp. 093510.
- G. E. P. Box; M. E. Muller** (1958): A Note on the Generation of Random Normal Deviates. *The Annals of Mathematical Statistics*, vol. 29, no. 2, pp. 610–611.
- H. Trumel et al.** (2009): On probabilistic aspects in the dynamic degradation of ductile materials. *J. Mech. Phys. Solids*, vol. 57, pp. 1980–1998.
- J. D. Lindl et al.** (2004): The physics basis for ignition using indirect-drive targets on the National Ignition Facility. *Physics of plasmas*, vol. 11, no. 2, pp. 339.
- J. S. Rinehart** (1952): Scabbing of metals under explosive attack: multiple scabbing. *J. Appl. Phys.*, vol. 23, pp. 1229–1233.

- L. Davison et al.** (1996): *High pressure shock compression of solids II - Dynamic fracture and fragmentation*. Springer, New York.
- L. Tollier; R. Fabbro** (1998): Study of the laser-driven spallation process by the VISAR interferometry technique. II. Experiment and simulation of the spallation process. *Journal of Applied Physics*, vol. 83, no. 3, pp. 1231.
- M. A. Meyers; C. T. Aimone** (1983): Dynamic fracture (spalling) of metals. *Prog. Mater. Sci.*, vol. 18, pp. 1–96.
- M. A. Meyers et al.** (2001): Plastic deformation in laser-induced shock compression of monocrystalline copper. In M. D. Furnish; N. N. Thadhani; Y. Horie(Eds): *Shock Compression of Condensed Matter*, pg. 619.
- M. Boustie; F. Cottet** (1991): Experimental and numerical study on laser driven spallation into aluminum and copper targets. *Journal of Applied Physics*, vol. 69, no. 11, pp. 7533–7538.
- P.-H. Maire** (2009): A high-order cell-centered lagrangian scheme for compressible fluid flows in two-dimensional cylindrical geometry. *Journal of Computational Physics*, vol. 228, pp. 6882–6915.
- P.-H. Maire; J. Breil** (2008): A second-order cell-centered lagrangian scheme for two-dimensional compressible flow problems. *International Journal for Numerical Methods in Fluids*, vol. 56, pp. 1417–1423.
- P.-H. Maire et al.** (2008): A cell-centred arbitrary lagrangian-eulerian (ale) method. *International Journal for Numerical Methods in Fluids*, vol. 56, pp. 1161–1166.
- S. Eliezer et al.** (1990): Laser induced spall in metals: Experiment and simulation. *J. Appl. Phys.*, vol. 67, pp. 715.
- S. Eliezer et al.** (1990): Shock wave decay and spall strength in laser-matter interaction. *J. Appl. Phys.*, vol. 68, pp. 356.
- T. Antoun et al.** (2002): *Spall Fracture*. Springer, New York.
- T. De Ressaiguier; M. Hallouin** (2008): Effects of the α - ϵ phase transition on wave propagation and spallation in laser shock-loaded iron. *Phys. Rev. B*, vol. 77, pp. 174107.
- T. De Ressaiguier et al.** (1997): Spallation of metals subjected to intense laser shocks. *Journal of Applied Physics*, vol. 82, no. 5, pp. 2617–2623.
- V. V. Silberschmidt** (2003): Crack propagation in random materials computational analysis. *Computational Materials Science*, vol. 26, pp. 159–166.
- V. V. Silberschmidt** (2006): Effect of material's randomness on scaling of crack propagation in ceramics. *International Journal of Fracture*, vol. 140, pp. 73–85.

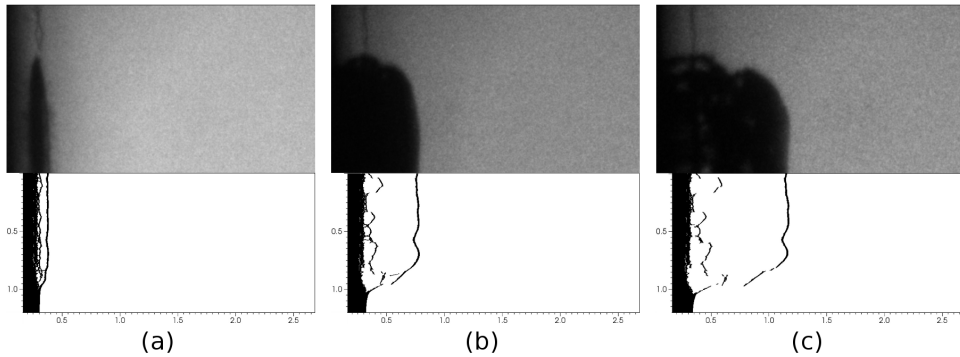
Appendix A: Comparison between experiments and simulations

Figure 15: Comparison between transverse shadowgraphs of fragments ejected from a 300 μm -thick gold target subjected 47 GPa laser shock and its corresponding 2D numerical simulation at different times after the laser shot: (a) 365 ns (b) 1790 ns (c) 3215 ns.

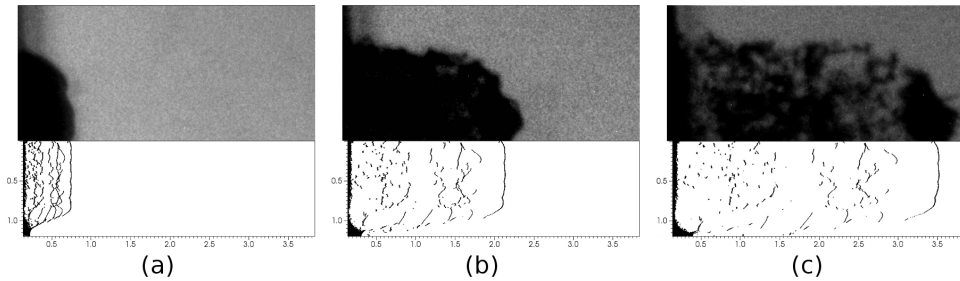


Figure 16: Comparison between transverse shadowgraphs of fragments ejected from a 200 μm -thick aluminium target subjected 46 GPa laser shock and its corresponding 2D numerical simulation at different times after the laser shot: (a) 365 ns (b) 1215 ns (c) 2065 ns

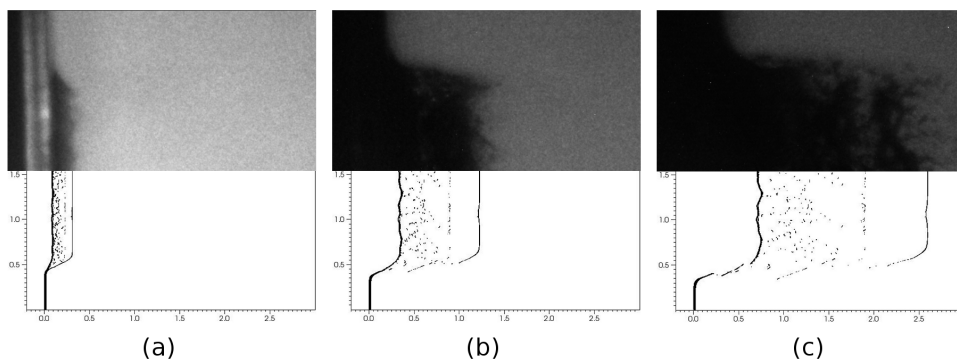


Figure 17: Comparison between transverse shadowgraphs of fragments ejected from a 20 μm -thick gold target subjected 36 GPa laser shock and its corresponding 2D numerical simulation at different times after the laser shot: (a) 365 ns (b) 1505 ns (c) 3215 ns

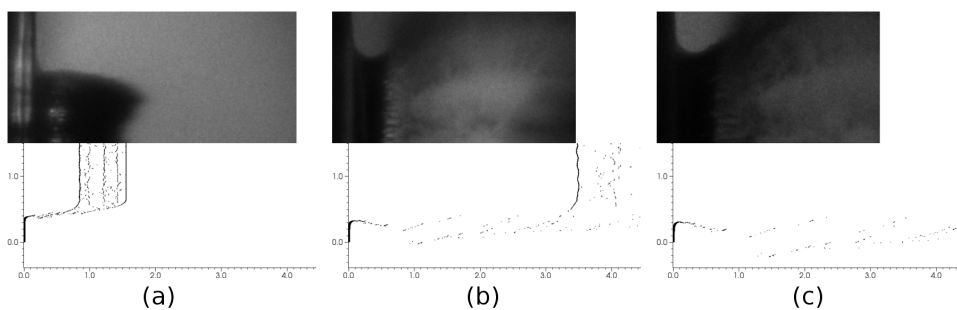


Figure 18: Comparison between transverse shadowgraphs of fragments ejected from a 20 μm -thick aluminium target subjected 61 GPa laser shock and its corresponding 2D numerical simulation at different times after the laser shot: (a) 365 ns (b) 1505 ns (c) 2075 ns

